JOURNAL OF GEOPHYSICAL RESEARCH, VOL. 117, C03031, doi:10.1029/2011JC007650, 2012

Wind-driven modification of the Alaskan coastal current

E. L. Shroyer[1,2] and A. J. Plueddemann[1]

Received 30 September 2011; revised 18 January 2012; accepted 23 January 2012; published 20 March 2012.

[1] Across-shelf transects over the eastern flank of Barrow Canyon were obtained in August 2005 with an autonomous underwater vehicle (AUV). Here, the shelf topography creates a "choke" point in which a substantial portion of Pacific inflow from the Bering Strait is concentrated within 30 km of the coast, providing an ideal setup for monitoring the flow with the AUV. Four transects, extending ~10 km offshore of Barrow, Alaska, inshore of the ~80 m isobath, were used in conjunction with a process-oriented numerical model to diagnose the wind-driven modification of the Alaskan coastal current. Poleward transports of 0.12 Sv were consistent among all sections, although the transport-weighted temperature was about 1°C colder in the transect obtained during peak winds. An idealized numerical model reproduces the observed hydrographic structure and across-shelf circulation reasonably well in that (1) winds were not sufficient to reverse the poleward flow, (2) upwelling was most pronounced in the nearshore, and (3) the onshore return flow occurred throughout the interior as opposed to the bottom boundary layer. The across-shelf circulation provides a possible mechanism for a meltwater intrusion observed on the offshore side of the AUV transect made during peak winds. Also of interest is that the observed anticyclonic shear was much stronger ($|\partial u/\partial y| > f$) than previously measured in the region.

Citation: Shroyer, E. L., and A. J. Plueddemann (2012), Wind-driven modification of the Alaskan coastal current, *J. Geophys. Res.*, *117*, C03031, doi:10.1029/2011JC007650.

1. Introduction

[2] Pacific inflow from the Bering Strait is a source of freshwater, carbon, and nutrients for the Arctic Ocean. Seasonally, transport through the Strait is at a maximum of roughly 1.3 Sv in summer (June–July) with minima near 0.3 Sv occurring in March and December [*Roach et al.*, 1995]. Higher-frequency variability in the transport is well modeled by considering the combination of the pressure head forcing between the Pacific and Arctic and local wind forcing [e.g., *Woodgate et al.*, 2005]. In winter, both the eastern and western channels of the Strait have relatively uniform temperature while salinity increases toward the west [*Roach et al.*, 1995]. By contrast, variability in summer is significant. Both Bering Sea water and Alaskan Coastal Water, composed of the warm, fresh Alaskan Coastal Current (ACC) and other Alaskan shelf water, enter on the eastern side of the Strait, while nutrient- and carbon-rich Anadyr Water is found on the western side [*Coachman et al.*, 1975; *Walsh et al.*, 1989; *Woodgate and Aagaard*, 2005].

[3] After transiting the Bering Strait, Pacific water tends to follow one of three topographically steered pathways through the shallow Chukchi Sea [e.g., *Winsor and Chapman*, 2004; *Weingartner et al.*, 2005; *Spall*, 2007]; these are represented schematically in Figure 1. The observations presented here were taken along a transect line extending to the northwest off Barrow, Alaska into Barrow Canyon found at the northeast corner of the Chukchi; as such, they are located in the easternmost transport branch. Barrow Canyon runs roughly parallel to the northwest coastline of Alaska. At Point Barrow, the coastline takes an almost 90° turn to the east so that the canyon intersects the Alaskan Beaufort Shelf, thereby connecting the Chukchi Sea with the deep Canada Basin (Figure 1). The complex bathymetry and coastline, combined with the variability in upstream conditions and winds, create a rich and complicated physical environment in the vicinity of Barrow Canyon.

[4] Not surprisingly, past observational studies have shown that both the flow field and water masses found in the canyon can differ greatly at a range of time and space scales [e.g., *Paquette and Bourke*, 1974; *Garrison and Paquette*, 1982; *Aagaard and Roach*, 1990; *Weingartner et al.*, 1998]. In the mean, flow through the canyon is northward toward the Beaufort Sea with transports that tend to be largest in late summer [*Woodgate et al.*, 2005]. However, the details of circulation within Barrow Canyon arise from a combination of the large-scale pressure gradient between the Pacific and Arctic [*Mountain et al.*, 1976], local wind forcing [*Weingartner et al.*, 1998; *Okkonen et al.*, 2009], topographic waves [*Aagaard and Roach*, 1990], hydraulic control [*Pickart et al.*, 2005], and (in summer) local buoyancy-driven dynamics associated with the ACC. The relative importance

[1]Woods Hole Oceanographic Institution, Woods Hole, Massachusetts, USA.
[2]Now at College of Earth, Ocean, and Atmospheric Sciences, Oregon State University, Corvallis, Oregon, USA.

0148-0227/12/2011JC007650

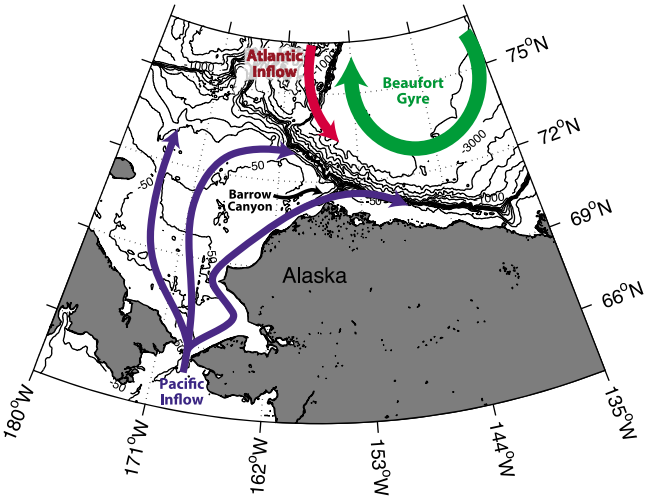

Figure 1. Schematic showing pathways of Pacific Water across the Chukchi Sea. The current study site is located just offshore of Barrow, Alaska, with a transect line extending into Barrow Canyon.

of these forcing mechanisms depends on the timescale of interest, the time of year, and the presence of ice cover. For example, winds may drive the relatively short-term variability, O (days) [*Weingartner et al.*, 1998], while long-term variability, O (months), is linked to the pressure head between the Pacific and the Arctic [*Woodgate et al.*, 2005].

[5] In this study, we focus on changes in coastal current structure on timescales of days in the presence of moderately strong wind events with minimal ice cover. Thus, the expectation is that local wind forcing is primarily responsible for the observed changes, with buoyancy forcing and the large-scale pressure gradient playing important roles. Studies detailing the response of the coastal ocean to local wind forcing have a long history (see review by *Winant* [1980]), while differences in meteorological forcing, oceanographic conditions (i.e., stratification, mean circulation), and geomorphology of different locations continue to drive observation and analysis [e.g., *Austin and Lentz*, 2002; *Pringle*, 2002; *Lentz and Chapman*, 2004; *Whitney and Allen*, 2009; *García-Reyes and Largier*, 2010]. In particular, the across-shelf response to wind forcing is highly variable for different regions, and even for the same region at different times. For example, *Lentz and Chapman* [2004] show that for large slope Burger numbers ($S = \alpha N/f$, where α is the shelf slope, N is the buoyancy frequency, and f is the Coriolis parameter), the onshore flow occurs in the interior of the water column as opposed to the bottom boundary layer. The alongshelf pressure gradient has also been attributed with playing an important role in setting both the vertical structure of the across-shelf flow as well as alongshelf response upon relaxation of winds [e.g., *Lentz and Winant*, 1986; *Davis and Bogden*, 1989; *Dever*, 1997; *Gan and Allen*, 2002; *Barth et al.*, 2005; *Chapman and Lentz*, 2005; *Lentz*, 2008]. Other efforts have explored the impact of across-shelf winds, which can be a significant contributor to the across-shelf momentum equation on the inner shelf [*Tilburg*, 2003; *Fewings et al.*, 2008], and stratification, which strongly influences the across-shelf location of upwelling [*Lentz*, 2001].

[6] In addition to wind forcing, buoyancy forcing plays a strong role in setting circulation in the coastal ocean. Studies that concentrate in the far-field regions of river plumes are analogous to the present data set, which samples through the warm buoyant Alaskan Coastal Current far downstream from its source. Details of the interplay between wind and buoyancy can be quite complicated [*Münchow and Garvine*, 1993], in part due to the range in parameter space (e.g., volume of buoyant outflow, wind strength and direction, shelf topography, etc.). Upwelling winds, like those observed in the present study, oppose the natural alongshelf tendency of plumes to move in the direction of coastally trapped waves and cause thinning and spreading of buoyant water [*Fong et al.*, 1997; *Fong and Geyer*, 2001; *Lentz*, 2004]. The presence of a plume also impacts how the coastal ocean responds to wind forcing since the buoyant water creates a low-density cap over the nearshore, trapping momentum flux near the surface and inhibiting outcropping of upwelled water [e.g., *Fong et al.*, 1997; *Hickey et al.*, 2005]. *Whitney and Garvine* [2005] introduced a wind strength index, defined as the ratio between pure wind-driven and buoyancy-driven alongshelf velocities ($W = u_{wind}(u_{buoyancy})^{-1}$), to distinguish between buoyancy- and wind-controlled regimes.

2. Present Study

[7] A Remote Environmental Monitoring Units (REMUS) autonomous underwater vehicle (AUV) was used for repeat sampling along a single transect line extending from the 10 to 80 m isobaths across the sidewall of Barrow Canyon. Of interest in these data is an observed alteration in the coastal current, in which one of the transects distinguished itself from the others in both the observed temperature-salinity (TS) properties and the across-shelf structure of the coastal current. The anomalous transect is characterized by the presence of a relatively fresh, cold middepth intrusion (attributed to mixed sea ice meltwater) at the offshore side of the transect and a pronounced subsurface maximum in the alongshelf current that is not found in the other transects. The shift is theorized to be associated with wind-driven across-shelf circulation, since the anomalous transect was acquired during a time of peak offshore/upwelling winds, whereas other transects were acquired during weak winds. The ability of the AUV to simultaneously measure density and velocity, combined with the premise that the meltwater intrusion serves as a useful tracer for transport, provides a unique opportunity to quantify the across-shelf response to wind forcing in this region.

[8] In order to form a basis for our understanding, we first quantify relevant nondimensional parameters for these data. In the survey region, the depth increases ~40 m every 5 km, which at 71 20′ N results in a slope Burger number of roughly $S \approx 0.6$. Across-shelf and alongshelf winds were comparable in magnitude; however, the ratio of the across-shelf wind stress (τ_y) to the Coriolis force of the alongshelf flow ($R = \tau_y(\rho h f\bar{u})^{-1}$, where ρ is the density of seawater, h the water depth, and $\bar{u}$ the depth-averaged alongshelf velocity) peaked at 0.3 for a depth of $h = 10$ m. The wind strength ratio, W, is estimated as ~0.5 based on a

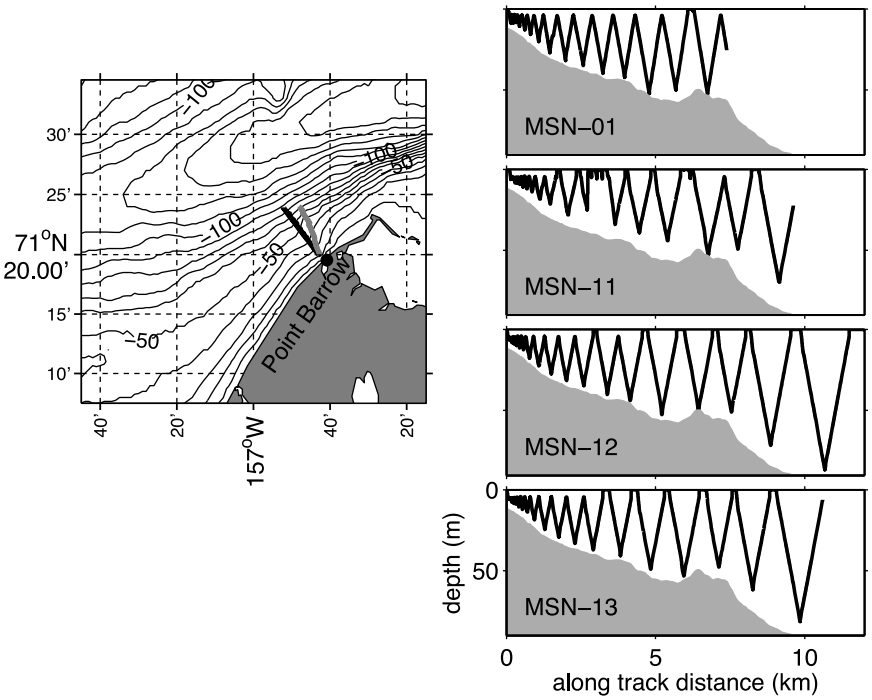

Figure 2. (left) Close-up of local bathymetry and AUV transect lines off Point Barrow. MSN-01, MSN-12, and MSN-13 followed the black line; MSN-11 followed the grey line. For MSN-11, ADCP data were not available, and the vehicle did not adjust its heading to account for advection by the current. (right) AUV paths through the water as a function of offshore distance.

$u_{buoyancy} \sim 0.5$ m s^{-1} calculated from the observed depth-averaged velocity under low wind forcing and a $u_{wind} = \sqrt{(\rho_{air}C_{10})(\rho C_D)^{-1}}U_{10} \sim 0.25$ m s^{-1}, where ρ_{air} is the density of air, $C_{10} = 1.2 \times 10^{-3}$ is the surface drag coefficient, $C_D = 2 \times 10^{-3}$ is the bottom drag coefficient, and $U_{10} = 10$ m s^{-1} is the peak alongshelf wind speed. (u_{wind} is calculated assuming a quadratic bottom stress in balance with the surface stress.) Based on these parameters we might expect that (1) the return flow may partially be distributed in the interior, (2) across-shelf winds are not important outside the mixed layer, and (3) the alongshelf velocity is in a buoyancy-driven state upon which the wind-forced response will be superimposed.

[9] Further description of the AUV and sampling scheme is given in section 3. Observations detailing the wind conditions during the experiment, the measured TS properties, and the across-shelf hydrographic and current structure are presented in section 4. Estimated current transports are given in section 5.1, and interpretation of the data, based on an idealized numerical model, is summarized in section 5.2. The meltwater intrusion, across-shelf transport, and implications of observed changes in coastal current structure are discussed in section 6. A summary is given in section 7.

3. Method and Instrumentation

[10] Considering the compressed across-canyon scale of the flow (the canyon axis is ~20 km from the coastline), the site's accessibility, and the range in water column depths (5–200 m), the site is well suited to monitoring with a small (0.2 m diameter, 1.6 m length) and portable (weight less than 50 kg) REMUS-100 AUV, which is capable of transiting at roughly 3 knots for time periods up to 12 h. For this project, the AUV was equipped with upward and downward facing acoustic Doppler current profilers (ADCPs), a WetLabs ECO-Puck FLNTU, and a Seabird SBE-49 pumped conductivity-temperature-depth (CTD) profiler. The sampling scheme of the AUV is quite flexible; the sensors, navigational system processing, and vehicle path through water may all be adjusted depending on the experiment design and intent. The present study's primary purpose was as an engineering test in preparation for an under ice deployment carried out in the spring of 2010. As a result, a variety of sampling and navigational schemes were tested, and only 4 of 13 missions were useful for the present study.

[11] The four AUV missions of interest, MSN-01, MSN-11, MSN-12, and MSN-13 (Figure 2), were conducted over the course of 1 week from 23 to 30 August 2005. MSN-12 was round-trip; that is, data were recorded both on the offshore and onshore legs; all other missions were one way. The AUV sampled CTD data at 5 Hz, ECO-puck data at 1 Hz, and (depending on the transect) ADCP data at either 0.2 or 1 Hz. In MSN-01, a 600 kHz ADCP was used (sampled at 0.2 Hz), and in MSN-12 and MSN-13, a 1200 kHz ADCP was used (sampled at 1 Hz). ADCP data were not acquired during MSN-11. The vehicle undulated within the water column, turning within a few meters of the bottom and surface (Figure 2, right). The resultant spatial resolution varied depending on the vehicle track and sampling rate. For example, the CTD resolution was roughly a few centimeters in the vertical and 400 m in the horizontal at middepth (i.e., 5–10 km in Figure 2).

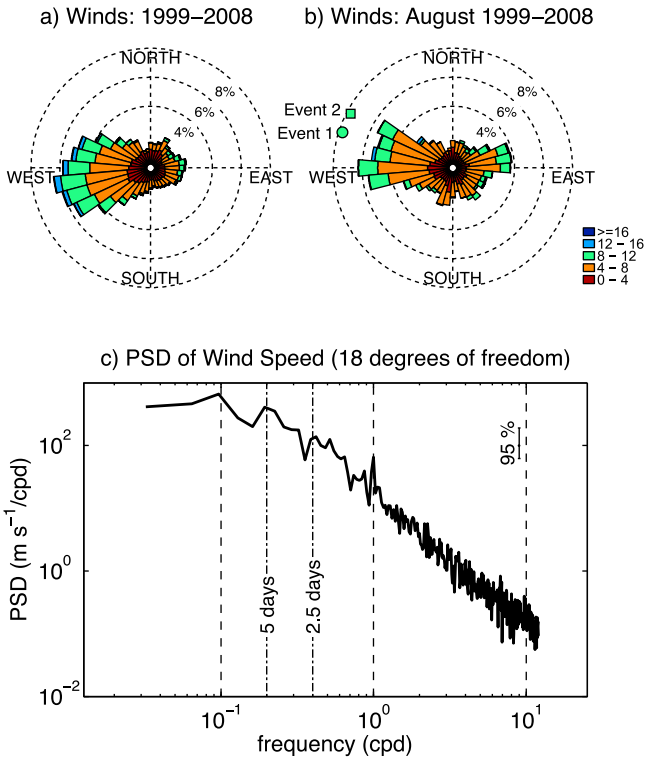

Figure 3. Polar histograms of wind speed and direction from (a) 1999 to 2008 and (b) August 1999 to 2008. Bars point in the direction that the wind blows toward. The data are hourly records from NOAA's Point Barrow Weather Station. Markers in Figure 3b show the direction of two wind events measured in late August 2005. The color of the markers is representative of the magnitude of the peak wind during each event, as indicated by the color scale. (c) Power spectral density (PSD) for the August wind records.

[12] Analysis of AUV velocity data indicated that several factors, including low scattering levels, high-noise floors (attributed to interference from the Inertial Navigation System), and multiple reflections, adversely affected quality. Data from the upward looking ADCP were disregarded entirely. The downward looking ADCP performed better, and provided bottom track data. Still, only the first ~3 bins consistently appeared to have good return strength.

[13] Data were corrected for vehicle movement using the bottom track velocity. When bottom track was not available, data were discarded. Given the depth range measured, this requirement influenced only near-surface values on the offshore side of the transect for the 1200 kHz ADCP. Data collected within 15% of the vehicle's distance to the bottom were disregarded to avoid sidelobe contamination. At each depth, a running (10 minute blocks) standard deviation filter was applied to remove data with absolute values twice the standard deviation. Georeferencing was checked by comparing the instrument path calculated from integrating the bottom track velocity to GPS fixes obtained at the surface.

[14] The first three bins were averaged together and a single velocity was calculated for each measurement time. A new depth value was assigned by adding the AUV depth and the average range of the first three bins; thus, the velocity record was transformed into a "point" measurement much like that of the CTD and ECO-puck data. For the 600 kHz unit, the result is equivalent to a 6 m vertical average made 4.5 m below the instrument every 10 s. For the 1200 kHz unit, the result is equivalent to a 1.5 m vertical average measure of velocity made 1.5 m below the AUV every 2 s. Note the factor of two difference between the time intervals given here and the sampling frequency (i.e., 0.1 and 0.5 Hz as compared to 0.2 and 1 Hz) is due to the fact that the sampling frequency is the combined rate of the upward and downward looking units, which ping alternately.

[15] Velocity (processed as described above) and CTD data were mapped onto vertical profiles by averaging successive up and down transits of the AUV into 1 m bins. Across-shelf distance was then taken as the average horizontal distance between up and down transits; across-shelf bins were therefore not uniform (varying from less than 50 m in shallow water to over 500 m in deep water). Velocity uncertainty, estimated using the precision from the ADCP manufacturer's documentation accounting for vertical and horizontal averaging, is 2–3 cm s^{-1}. Estimated errors for vertical shear, transport, and relative vorticity are 0.01–0.02 s^{-11}, 4–6 m^3 s^{-1}, and 4–6 $\times$ 10^{-5} s^{-1}, respectively.

[16] For MSN-11, velocity was calculated using the thermal wind shear referenced to the surface velocity, which was assumed equal to the velocity of the AUV calculated from GPS fixes during periods of free drift at the surface. Applying a similar technique to other transects shows reasonable agreement between the measured velocity and the geostrophic velocity referenced to surface drift. For example, surface drift in MSN-12 was estimated between 0.12 and 0.14 m s^{-1} while near-surface (<5 m) ADCP estimates were between 0.13 and 0.19 m s^{-1}. The greatest disparity was between an estimated 0.30 m s^{-1} drift velocity and 0.40 m s^{-1} measured velocity in MSN-13.

[17] Across-shelf and alongshelf were defined relative to the AUV transect line, which was aligned perpendicular to the coastline and nearshore isobaths (Figure 2). The positive x axis (positive u velocity) is directed alongshelf (down canyon) toward the northeast. The positive y axis (positive v velocity) is directed offshore.

4. Observations

4.1. Meteorological Conditions

[18] Figures 3a and 3b show polar histograms of hourly winds measured at the NOAA Point Barrow station from 1999 to 2008. Bars point in the direction to which the wind blows. Winds in August tend to be slightly weaker than the yearly average and directed toward the west-northwest as opposed to the west–southwest (compare Figures 3a and 3b). Elevated energy is present at the daily cycle as well as at periods of a few days (Figure 3c). The two wind events that were measured during this experiment period (Figure 3b, markers) are typical (i.e., similar magnitude, direction, and duration) for August.

[19] A detailed record from August 2005 shows the two relevant wind events, one near 00:00 UTC 24 August 2005 and the other peaking at 21:00 UTC 28 August 2005 (Figure 4). The peak wind stress for the second event (0.20 N m^{-2}, 11.5 m s^{-1}) was about 30% larger than that of the first event (0.15 N m^{-2}, 9.5 m s^{-1}) (Figure 4a). In

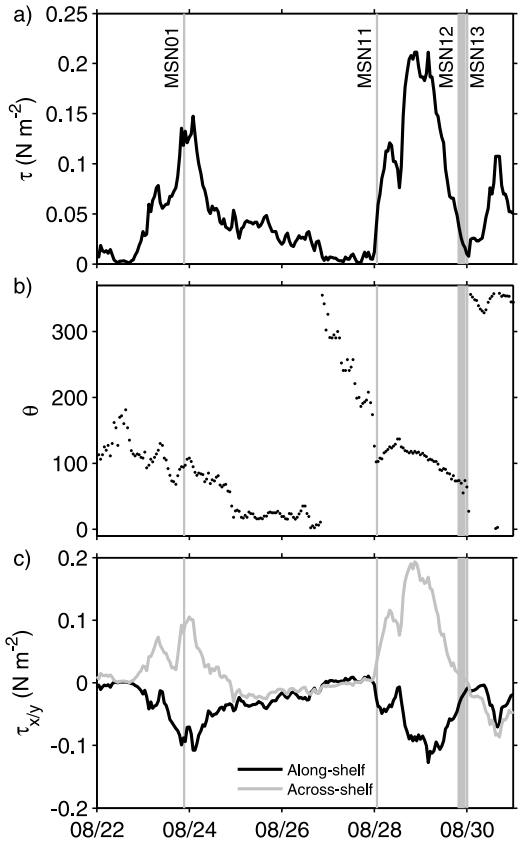

Figure 4. (a) Total wind stress, (b) wind direction, and (c) alongshelf (black) and across-shelf (grey) wind stress. Times of AUV transects are highlighted in light grey.

both cases, winds were from the east–southeast (Figure 4b), which at the transect location corresponds to an upwelling-favorable alongshelf component and an offshore across-shelf component (Figure 4c). Each event lasted roughly 2 days and had a similar timescale for the ramp-up and rapid initial decay. Winds were calm (<1 m/s) for ~1 day prior to both events.

[20] The first mission, MSN-01, occurred near the peak of the first wind event (Figure 4). MSN-11 took place approximately 4 days later during a period of weak forcing just prior to the second wind event. The final two missions, MSN-12 and MSN-13, were conducted back to back (start times separated by approximately 4 h) just after wind speeds relaxed from the second peak. The TS properties and across-shelf structure measured during these two missions were nearly identical. Henceforth, we show data from only MSN-13 and describe the characteristics of MSN-12/13 together.

[21] Assuming that (1) winds were a primary driver of variability in the across-shelf current and hydrographic structure over this short time frame and (2) the oceanic response to the two wind events should be similar, we consider MSN-01 to be representative of the state during peak winds, MSN-12/13 representative of the state early in the relaxation process, and MSN-11 representative of the state later in the relaxation process. Although factors other than the local winds may influence variability (e.g., coastally trapped waves, variability in the alongshelf pressure gradient, and/or advective influences from upstream), analysis of the response to wind forcing in section 5 supports this general premise. Continuing through the remainder of the paper, MSN-01 is referred to as the "Peak Wind" state, MSN-13 as the "Post Wind I" state, and MSN-11 as the "Post Wind II" state. Transects will therefore be discussed in relation to wind events and not in chronological order.

4.2. TS Relationships

[22] Three water mass modes were identified in these data (Figure 5): Chukchi Summer Water (CSW), Alaskan Coastal Current (ACC) water, and mixed meltwater (MW). CSW is likely the result of seasonal freshening and warming of Bering Winter Water (BWW) [*Weingartner et al.*, 2005; *Woodgate et al.*, 2005], which is a relatively well defined water mass with salinity between 32.5 and 33.5, and temperature near the freezing line [e.g., *Aagaard and Roach*, 1990; *Weingartner et al.*, 2005; *Pickart et al.*, 2005]. The grey arrow in Figure 5 schematically represents this summer transition and its proposed relation to the CSW mode. Historically, ACC water is well defined, although not as constrained in TS space as BWW. The salinity of the ACC may be as fresh as 30–31, and the temperature may exceed 5°C [*Woodgate and Aagaard*, 2005; *Woodgate et al.*, 2005]. As the warmest and freshest water mass, ACC water is easily distinguished at the upper left corner of TS space (Figure 5). (In this paper the term ACC is used to refer to water in a certain TS class; the coastal current offshore of Barrow, Alaska, is not necessarily solely composed of ACC water. In fact, all of the TS data shown in Figure 5 occur within the

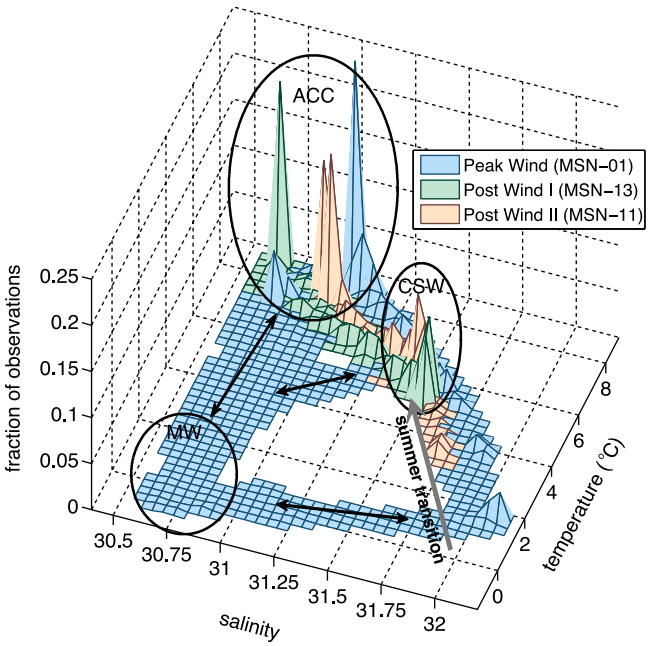

Figure 5. TS histograms for MSN-01, MSN-13, and MSN-11. Black arrows show mixing paths from the mixed meltwater (MW) region. Grey arrow represents the summer transition in TS space from Bering Winter Water (BWW), which would occupy the region just off axis of the lower right corner. Alaskan Coastal Current (ACC) peaks and Chukchi Summer Water (CSW) peaks are indicated.

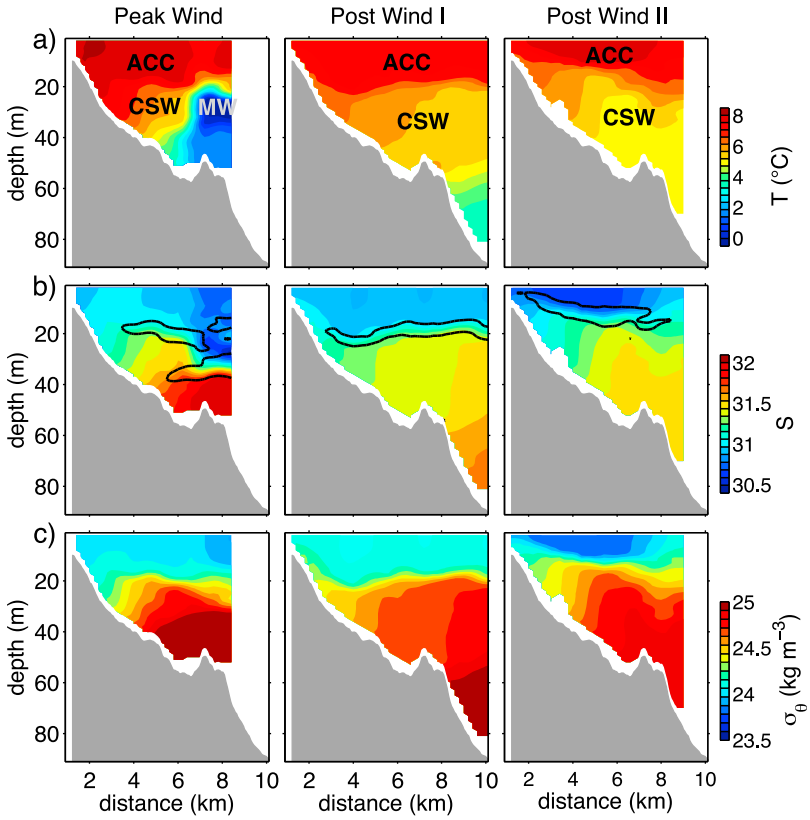

Figure 6. Across-shelf structure of (a) temperature, (b) salinity, and (c) potential density for the Peak Wind (MSN-01), Post Wind I (MSN-13), and Post Wind II (MSN-11) states. General locations of ACC, CSW, and MW are labeled in Figure 6a; $N^2 = 5 \times 10^{-4}$ is contoured in black in Figure 6b.

coastal current.) The cold, fresh corner of the TS space (lower left corner in Figure 5) is termed mixed meltwater (MW) based on its relative low salinity, temperature, and optical backscatter (not shown). Although chemical tracer information (e.g., oxygen isotopes) is not available to conclusively show this water has origins from ice melt, this classification is supported circumstantially considering (1) the transect location on the eastern Chukchi shelf, which is removed from riverine influence and upslope of surface freshwater found in the Beaufort Sea and (2) satellite imagery revealing the presence of sea ice offshore of the transect during the observational period.

[23] The dominant mode in all transects is ACC water (Figure 5). For the Peak Wind transect (MSN-01) the maximum of the TS distribution occurs near 8.5°C and 31 salinity. For the Post Wind I state (MSN-13) the maximum is near 7.5°C and 30.9 salinity. For the Post Wind II state (MSN-11), the maximum is near 8.5°C and 30.7 salinity. Although shifted slightly in TS space, both Post Wind transects also show peaks at the upper end of the CSW at roughly 5–6°C and 31.5 salinity. For the Peak Wind transect, the CSW branch was relatively well distributed in TS space. MW was only observed in the Peak Wind state. Mixing lines between MW and CSW below, and between MW and ACC above are also apparent.

4.3. Across-Shelf Structure

[24] The across-shelf structure of temperature, salinity, and potential density during the different wind states, Peak Wind, Post Wind I, and Post Wind II, are shown in Figure 6; the current structure is shown in Figure 7.

4.3.1. Hydrographic Conditions

[25] As discussed above, the Peak Wind transect is distinguished by the presence of relatively cold and fresh meltwater (Figures 6a and 6b, left). The MW is confined to a middepth intrusion at roughly 30 m depth on the offshore side of the transect. In this transect, ACC water occupies the surface layer and fills the water column inshore of the ~30 m isobath. CSW extends from midtransect to beneath the MW intrusion on the offshore side, where water near the bottom has a similar temperature but greater salinity than the MW intrusion. The across-shelf density structure, corresponds to a positive thermal wind shear in the lower half of the water column and negative in the upper half of the water column near the 6 km mark (Figures 6c and 7c). A well-mixed wedge of fluid is located inshore of ~2 km; upwelling of isopycnals is not as apparent in this mission compared to the other transects. A region of elevated stratification ($N^2 = 5 \times 10^{-4}$s^{-2} contoured in black, Figure 6b) is observed at roughly 20 m depth offshore ~3 km as well as beneath the MW intrusion.

[26] Roughly 1 day (two inertial periods) after peak wind (Post Wind I), deep isopycnals (CSW) are upwelled along the coast (e.g., between 1 and 4 km in Figure 6c, middle). Even though the wind has ceased at this time, the wind-driven response has not yet decayed. The upwelling of isopycnals in the Post Wind I state is, in fact, greater than that in the Peak Wind state; that is, upwelling is a cumulative

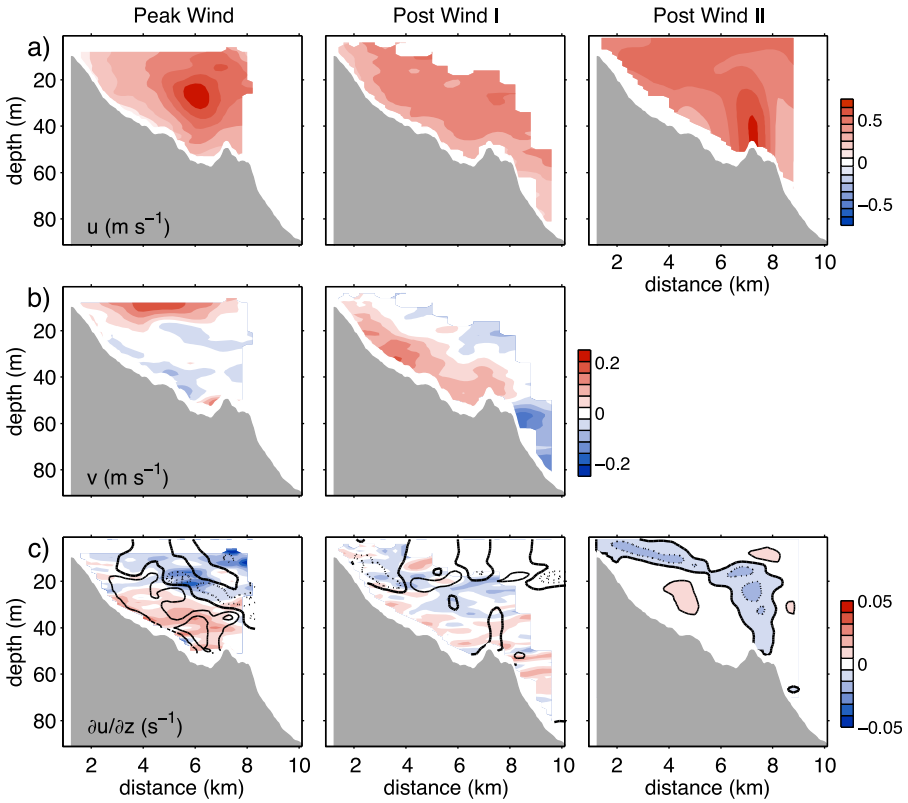

Figure 7. (a) Alongshelf and (b) across-shelf ADCP velocity for the Peak Wind (MSN-01), Post Wind I (MSN-13), and Post Wind II (MSN-11) states. Velocity data were low-passed filtered at 0.2 m^{-1} in the vertical and 1 km^{-1} in the horizontal before plotting. (c) Shear from ADCP data is shown by colored shading for the Peak Wind and Post Wind I states. Black contours show the thermal wind shear from density data. Contours are plotted in intervals of 0.02 s^{-1} with the zero contour indicated by the thick line and positive/negative values indicated by solid/dashed lines, respectively.

process that occurs throughout the wind event. The thermal wind shear is mostly negative shoreward of ~4 km, consistent with that expected for the upwelled isopycnals (Figures 6c and 7c). The thermal wind shear is weakly positive (particularly at depth) offshore of 4 km. This is attributed to the presence of the strong northward flow, which results in "down-turned" isopycnals in the bottom boundary layer. A strong pycnocline (black contour, Figure 6b) exists between the near-surface ACC and CSW at depth.

[27] Four days (roughly 8 inertial periods) after peak wind, upwelled isopycnals are still evident in shallow water (Post Wind II, Figure 6, right). However, in deeper water, isopycnals slope downward toward the bottom. The lowest salinity and highest temperature in the ACC was observed during the Post Wind II state (Figures 6a and 6b), and as such the potential density near the surface is less than values measured in the other missions. As with the Post Wind I state, the highest stratification is found between ACC located near the surface and CSW found at depth. The thermal wind shear is positive at depth and near the surface. Regions of negative thermal wind shear were located in the nearshore (~3 km, 10 m depth) and over a topographic rise near 8 km (Figures 6c and 7c).

4.3.2. Coastal Current Structure

[28] Velocity data acquired during the Peak Wind state show a well-defined subsurface jet (Figure 7a, left), consistent with the thermal wind shear. The maximum velocity in the core of the jet was 0.77 m s^{-1}. In contrast, a well-defined current structure was not evident (Figures 7a, middle, and 7a, right) during the relaxation process. Using the measured thermal wind shear to extend velocity data to the surface indicates that near-surface velocities exceeded 0.5 m s^{-1} on the offshore edge of the transect during the Post Wind I state. The velocity field during Post Wind II state, which was reconstructed from the thermal wind shear, suggests a more complicated structure with a mean velocity of 0.5 m s^{-1} alongshelf toward the northeast (Figure 7a, right). A bottom-intensified region is apparent over the topographic rise, associated with the bowing of isopycnals over this small feature. In contrast to estimations made by *Weingartner et al.* [1998], these data do not show reversals in the along-canyon current even though wind speed exceeded 6 m s^{-1}. The difference may be attributed to the relatively short duration of the observed wind events and the location of the AUV transect line in relation to the *Weingartner et al.* [1998] data set.

[29] For the Peak Wind state, the measured vertical shear (Figure 7c) is negative in the upper ~20 m with minima occurring above the shoreward side of the current core (−0.038 s^{-1}) and near the surface on the offshore edge of the transect (−0.045 s^{-1}). The shear is positive (~0.025 s^{-1}) in the lower half of the current. The observed structure is in

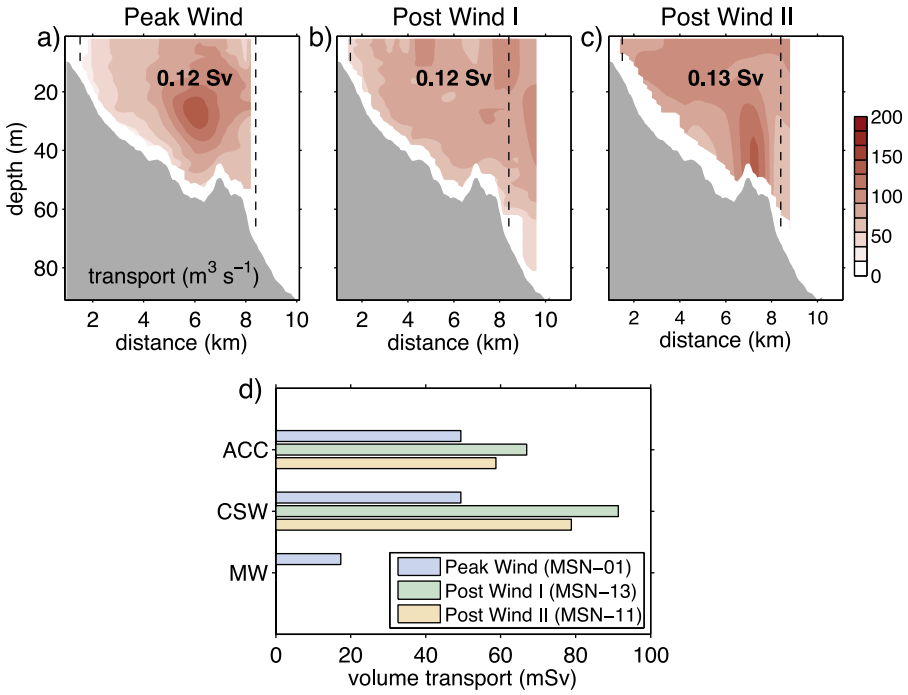

Figure 8. Estimated alongshelf transport for the (a) Peak Wind, (b) Post Wind I, and (c) Post Wind II states. In the Peak Wind and Post Wind I states, ADCP data were extended to the surface using thermal wind shear before calculating transport. In the Post Wind II state, thermal wind shear was referenced to the surface velocity to calculate the total velocity field. Total transport (integrated between dashed lines) is given in sverdrups. (d) Alongshelf transport of ACC, CSW, and MW in each wind state. Note here the entire domain is considered, as opposed to regions encompassed by dashed lines in Figures 8a–8c.

good agreement with the thermal wind shear (black contours, Figure 7c). For the Post Wind I state, both the measured and thermal wind shear are weak with a poorly defined structure, but the general features are similar. For example, measured and thermal wind shear are both positive near the bottom and both negative shoreward of ~4 km.

[30] Although the nearshore current structure was nearly uniform early in the relaxation process, it is possible that the core of the current was located offshore of the AUV transect. Furthermore, despite the presence of the well-defined core observed during peak winds, it is not certain that another maximum did not exist further offshore. Comparison of the AUV transects to observations from previous studies (e.g., Figure 3b of *Pickart et al.* [2005], which shows a current centered over the 125 m isobath), suggest that it is likely that the current extends well offshore of the range presented here. (Note that the *Pickart et al.* [2005] transect was located closer to the mouth of the canyon than the AUV transect line.) However, another perspective is presented by *Okkonen et al.* [2009], who summarize current structure under varying wind conditions. Near the location of the AUV transect line, these authors show that the across-shelf structure of the current can vary considerably. In one state [*Okkonen et al.*, 2009, Figure 7], they show a current with maximum velocity offshore of the 100 m isobath, similar to *Pickart et al.* [2005]; but in another [*Okkonen et al.*, 2009, Figure 6] the across-shelf velocity is characterized by multiple reversals, i.e., moving to the NE in the nearshore, to the SW between the 25 and 100 m isobaths, and then back to the NE across the center of the canyon.

[31] For this study, we assume that variability in the across-shelf velocity structure (Figure 7b) is primarily a wind-driven response (see section 5). During peak upwelling/offshore winds, an offshore flow was measured near the surface with a return flow below. The onshore flow was located both in the interior and near the bottom. In contrast, the across-shelf flow in the bottom boundary layer was offshore early in the relaxation process (Post Wind I state, Figure 7, middle), while the interior flow was relatively weak and directed onshore.

5. Analysis

5.1. Transport

[32] The estimated alongshelf transports (Figures 8a–8c), integrated from 1.5 to 8.5 km, are 0.12 Sv for the Peak Wind state, 0.12 Sv for the Post Wind I State, and 0.13 Sv for the Post Wind II state. Transports were calculated by extending velocity to the surface using the thermal wind shear and integrating over the smallest domain measured (i.e., the Peak Wind state). Transports for the different water masses (Figure 8d) were calculated by dividing TS space as follows: the ACC region encompasses salinity less than 31.25 and temperature greater than 6°C, CSW includes all other water located along the main ridge (i.e., the ridge lying parallel to the "summer transition" arrow in Figure 5), and MW encompasses water located off this ridge.

[33] In the Peak Wind state (blue, Figure 8d), transport of ACC and CSW are roughly the same, and about 3 times larger than the transport of MW. In the Post Wind I state

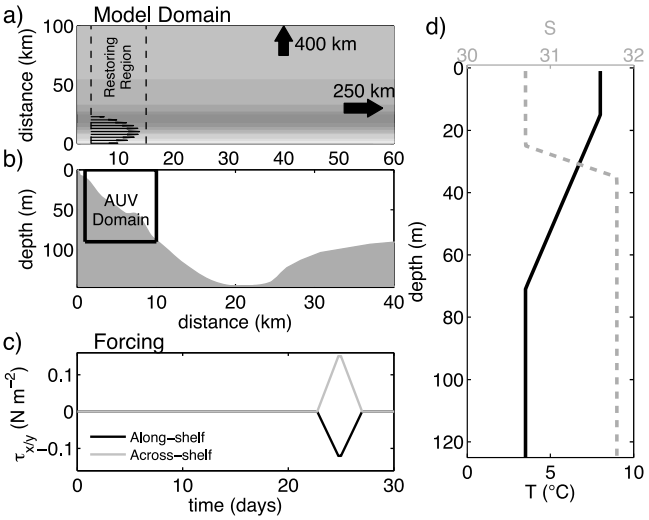

Figure 9. (a) Model domain, (b) bathymetric profile, (c) wind forcing, and (d) initial temperature (black) and salinity (grey) profiles. In Figure 9a, grey shading represents bathymetric contours with darker shades corresponding to deeper water. Note that the domain extends an additional 300 km offshore (total width 400 km) and the along-channel length is in total 250 km. The area isolated by vertical dashed lines indicates the restoring region where the along-channel velocity is forced to a barotropic current with across-shelf structure represented by the black arrows. The maximum current magnitude is 0.5 m s^{-1}.

(green, Figure 8d), transport of CSW is roughly 1.4 times that of ACC water even though ACC water occupies more of the domain (Figure 5). Although the transport is nearly barotropic (Figure 8b), the magnitude increases toward the offshore side of the domain, where the water column is composed of more CSW than ACC water. For the Post Wind II state (orange, Figure 8d), the peak transport occurs at depth, where CSW is the primary water type, and the transport of CSW is also about 1.4 times greater than transport of ACC water .

[34] Based on a collection of summer/fall CTD surveys, *Woodgate and Aagaard* [2005] estimate that roughly 0.2 Sv of ACC water enters at the Bering Strait. They extend this seasonal estimate using the annual mean velocity collected at a long-term mooring in the Strait and arrive at an annual mean volume transport of slightly less than 0.1 Sv. Using the limits defined above, we estimate between 0.05 and 0.07 Sv of ACC water in these transects. Reasonable agreement between our transport estimates and those at the Bering Strait suggests continuity (at least intermittently) in the ACC along the coast of Alaska as far north as Point Barrow. Considering the number of processes that may influence the ACC water in route through the Chukchi and realizing the limitations associated with the offshore extent of the AUV transect line, difference between our "snapshots" and *Woodgate and Aagaard*'s [2005] seasonal estimate is not surprising.

[35] Interestingly, the extension of the CSW ridge in the Peak Wind state to cooler, saltier water in comparison to that of the other missions results in the transport-weighted average temperature for this mission being $O(1)$ degree cooler than that of either the Post Wind states. Specifically, the transport-weighted temperatures are 5.8°C, 6.6°C, and 64°C for the Peak, Post Wind I, and Post Wind II states, respectively. The transport weighted salinities were similar at 31.27, 31.25, 31.22 for the Peak, Post Wind I, and Post Wind II states, respectively.

5.2. Wind-Driven Response

5.2.1. Model Setup

[36] In order to substantiate the premise that across-shelf variability was primarily wind driven, a simple, process-oriented model was used to interpret the across-shelf density and velocity field. The MIT general circulation model [*Marshall et al.*, 1997] was run in a channel configuration with periodic boundary conditions in the along-channel direction and closed walls at the sides of the channel (Figure 9a). The horizontal resolution was set to a constant 5 km in the along-channel direction, and varied between 250 m near the "canyon" and 10 km over the shelf in the across-channel direction. A vertical resolution of 2 m was used throughout.

[37] The across-channel bathymetry is realistic. AUV measured bathymetry was smoothed so that features smaller than ~200 m were neglected, and data were extended outside the AUV domain using a slope characteristic of Barrow Canyon and the Chukchi shelf (Figure 9b). The wall on the offshore side of the channel was extended out to 400 km to ensure that this remote boundary did not influence the wind-driven coastal upwelling response. Topographic variations in the alongshelf direction are neglected.

[38] A restoration region (Figure 9a) was used to force a depth-independent, along-channel flow of the form

$$u_0(y) = 0.5 \text{ m s}^{-1} - \{(y - 10000 \text{ m})/20000 \text{ m}\}^2.$$

Negative velocities were not imposed, instead $u_0(y)$ was set equal to zero when the quadratic is negative. The velocity was restored over a timescale, τ, according to $\tau^{-1}\Delta u$ where Δu is the difference between the model velocity and u_0. τ was varied from 30 min to 12 h; results presented here are for τ = 3 h. The resultant current is intended to mimic that off the northwest coast of Alaska where, in the absence of wind forcing, water flows poleward.

[39] The model temperature and salinity fields were idealized using the observed data (Figure 9d). Both fields consisted of homogeneous layers near the surface and bottom. The thermocline/halocline was created using a linear interpolation between the surface and deep temperature/salinity values. Isotherms/isohalines were initially flat, and the model was initialized from rest. Temperature, salinity, and across-shelf velocity were allowed to freely develop (i.e., no restoration was imposed).

[40] A quadratic drag law with $C_D = 2 \times 10^{-3}$ was applied at the bottom. The horizontal eddy diffusivity and viscosity were set to a constant 5 m^2 s^{-1}. The model was configured to use the K profile parameterization vertical mixing scheme [*Large et al.*, 1994] with a background diffusivity/viscosity of 10^{-5} m^2 s^{-1}. No heat flux was allowed through the surface or the bottom. The surface boundary condition was set by the wind stress (Figure 9c), which was not imposed until day

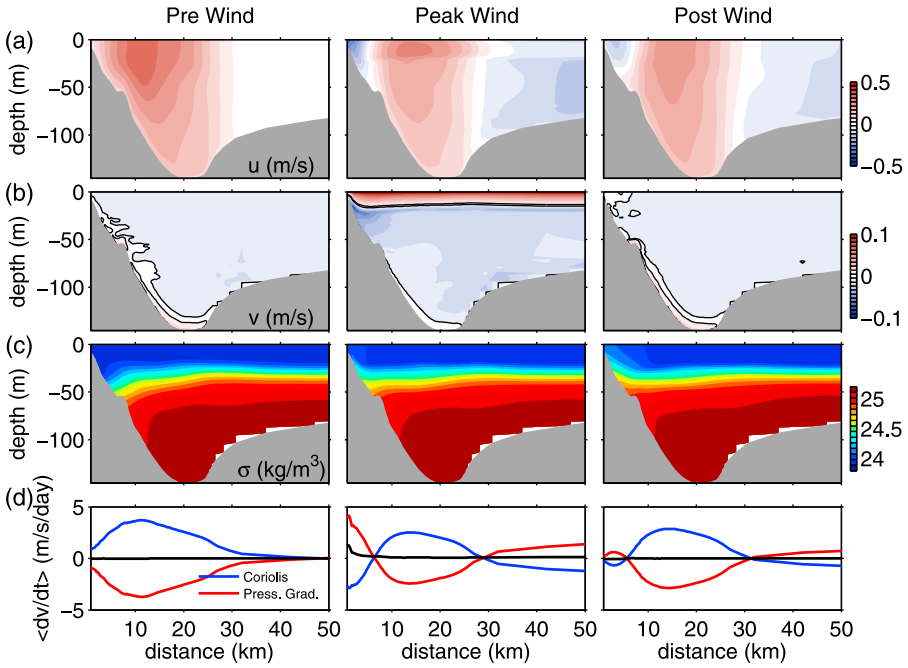

Figure 10. (a) Modeled along-channel velocity, (b) across-channel velocity, and (c) density for the time prior to the wind event, at peak wind, and after winds were turned off. Sections are compiled using the along-channel average x = 150–200 km. Contours show 0 and 1 cm s^{-1} in the across-channel velocity. (d) Depth-averaged, across-channel pressure gradient (red), Coriolis force (blue), and sum of the two terms (black).

22.75. By this time, the current forced by the restoration region had reached a near-steady geostrophic balance.

5.2.2. Model Results

[41] Modeled along-channel velocity (u), across-channel velocity (v), and density (σ) are plotted in Figures 10a–10c. Cross sections were compiled from the average of fields between x = 150 and 200 km. (Analysis of surface pressure fields indicates that by this distance the current is well adjusted and not strongly influenced by the restoration region.) Prewind, the quasi-steady current is in geostrophic balance (Figure 10d). Vertical shear is introduced via bottom stress. Isopycnals slope downward into the bottom boundary in thermal wind balance with the vertical shear. A well-mixed region is formed inshore of roughly 5 km. A near-bottom stress layer, with flow directed offshore, is apparent in the model data between y = 10 and 25 km. Inshore of this region, offshore flow is very weak, and the bottom boundary layer has almost "shutdown" [e.g., *Garrett et al.*, 1993]. A weak shoreward flow, balanced by an along-channel pressure gradient (see discussion below), is found in the interior of the water column. In one model run, the spin-up period was allowed to continue for an additional 10 days; no appreciable difference in the Pre Wind state was observed.

[42] In the Peak Wind state, the overall magnitude of the geostrophic current has reduced (Figure 10a, middle). Near the shore the current has reversed. An opposing flow is also formed offshore. The surface Ekman response results in a larger reduction in u near the surface than at depth. The offshore Ekman flow is clearly evident in the across-shelf response. The return flow is continuous across the channel at the base of the Ekman layer, and a weak return flow is observed throughout the interior. Return flow in the bottom boundary layer is confined to regions where the current reversed; the bottom boundary layer between 10 and 25 km still transports water offshore (Figure 10b, middle). This feature is not surprising since, in the traditional upwelling problem, the return flow in the bottom boundary layer results from the development of a stress layer for an interior u directed with the upwelling winds [*Allen*, 1973]. Upwelling of isopycnals is primarily confined to the inshore region (Figure 10c, middle). The balance is geostrophic offshore of ~5 km (Figure 10d, middle); frictional forces (not shown) are important in the nearshore.

[43] The magnitude of u is reduced in the Post Wind state, as compared to that before the wind is applied. The reversal near the shore is not as strong (Figure 10a, right). v is weak and resembles that of the Pre Wind state (Figure 10b, right). Upwelling of isopycnals has increased relative to the Peak Wind state (Figure 10c, right). As before, upwelling is greatest in the nearshore; offshore, isopycnals bend down into the bottom boundary layer consistent with the thermal wind shear in the interior flow. The across-shelf momentum balance is geostrophic (Figure 10d, right). In contrast to the Pre and Peak Wind states, the Post Wind state is sensitive both to the restoration timescale imposed as well as the length of the channel. (Although only the results for the case with a channel length of 250 km are presented, runs of various lengths between 50 and 250 km were tested.)

[44] Examination of the alongshelf momentum balance lends further insight (Figure 11). Before winds are imposed, the model reaches a steady balance, such that the loss of momentum to bottom stress (green line, Figure 11a) is balanced by forcing in the restoration region (magenta line, Figure 11a). Although artificially imposed, this external

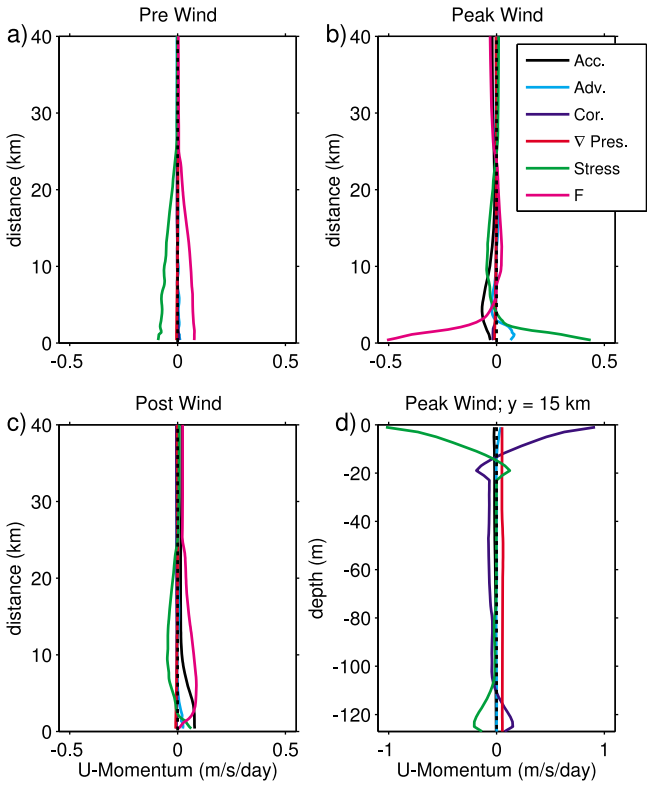

Figure 11. The across-shelf variation of the depth-averaged, alongshelf momentum budget in the modeled (a) Pre Wind, (b) Peak Wind, and (c) Post Wind states. Lines in Figures 11a–11c represent the alongshelf average over the entire domain, including the restoration region. Shown are acceleration (black), advection (cyan), Coriolis force (blue), pressure gradient (red), stress (green), and external forcing (magenta). (d) Alongshelf momentum budget at y = 15 km. Note in contrast to Figures 11a–11c, Figure 11d is an average between x = 150 and 200 km (excludes restoration region). The green line in Figure 11d is a combination of the stress and the external forcing, which is solely attributable to wind forcing since the averaging area is located outside the restoration region. Because wind stress is applied only to the uppermost cell, the presentation is simplified by combining these two components. The black dashed line highlights the zero crossing in Figures 11a–11d.

force mimics an alongshelf pressure gradient in the coastal ocean, and between x = 150 and 200 km a model generated alongshelf pressure gradient is found (red line, Figure 11d). Closer to the restoration region the pressure gradient is considerably larger with a complicated structure. *Chapman and Lentz* [1997] offer a detailed look at the acceleration of a current over a sloping bottom. The response of our model is similar to the results presented by these authors in the region just downstream of the restoration region.

[45] During peak upwelling/offshore winds (Figure 11b), the depth-averaged, alongshelf momentum balance is primarily between external forcing (a combination of wind stress and the restoring force), bottom friction, advection (in the nearshore), and acceleration. Note that inshore of roughly 5 km, the external forcing (magenta line) is opposite that of the Pre Wind state, and is primarily associated with the wind forcing as opposed to the restoration force. At this point, deceleration (black line) of the current has slowed near the coastal wall, but is stronger further offshore. The balance immediately after winds cease (Figure 11c) shows that the system is quickly "resetting" to the Pre Wind configuration. The current is accelerating (black line), and, the stress (green line) and external forcing (magenta line) act primarily in the same direction as that of the Pre Wind state.

[46] Figure 11d shows the momentum budget as a function of depth during the Peak Wind state at a distance located 15 km from the coastal wall. In this case, the alongshelf average is performed from 150 to 200 km and *does not* include the restoration region, so that external forcing is solely attributed to winds. Also, the external forcing and the stress are combined and shown as a single green line; this is done merely for ease of interpretation since the wind stress is only imposed in the upper most cell (i.e., plots as a scaled delta function at the surface). Surface and bottom Ekman layers, where stress (green line) is primarily balanced by the Coriolis term (blue line), are present. In the interior the balance is roughly geostrophic between the alongshelf pressure gradient established by our model configuration and a weak return flow onshore. The stronger return flow located at the base of the surface Ekman layer (Figure 10b, middle) is a result of both the across-shelf and alongshelf wind stress. (Model runs forced with alongshelf winds alone do not result in such a pronounced structure.) Note also that the stress in the surface and bottom layers are in the same direction, since this is a location where the alongshelf current has not reversed.

[47] Model cross sections constrained to the region sampled by the AUV are shown in Figure 12. Several similarities can be seen between the observed data and the modeled across-shelf velocity (Figure 12a) and density structure (Figure 12b). During the Peak Wind state, the model shows the development of the near-surface, offshore Ekman flow with a return flow that is distributed throughout

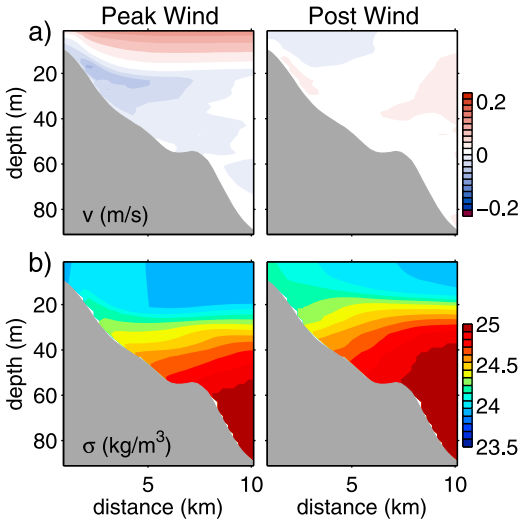

Figure 12. (a) Modeled across-shelf velocity and (b) density for Peak Wind and Post Wind state. Only the AUV domain is plotted; sections are compiled using an along-channel average (25 km) outside the restoration region.

the interior. This result is consistent with work by *Lentz and Chapman* [2004] for a slope Burger number greater than 0.5. In the Post Wind state, a weak offshore flow is apparent near the bottom, similar, but considerably less than that observed. The velocity response in the Post Wind state is sensitive to model parameters (restoration timescale and domain length), as mentioned previously, and the magnitude/direction of v varies depending on configuration.

[48] The location of the return flow during peak winds, in particular the maxima found at the base of the surface Ekman layer, is a robust response."Traditional looking" upwelled isopycnals are found close to shore; and, in regions where the current did not reverse, isopycnals turn into the bottom. The effect of the wind is to introduce vertical structure to the near-surface portion of the current. That is, in this case (with the given magnitude/structure of the current compared to the wind forcing), the wind forcing tends to reduce the alongshelf, near-surface velocity more so than the velocity at depth; the current structure is modified so that the surface maximum becomes a subsurface maximum.

6. Discussion

[49] Given the construct of the model, it is important to note its limitations and rationale. Not surprisingly, the downstream structure of u is strongly influenced by the current form imposed in the restoration region. Simulations were run with both the quadratic form defined above, as well as a Gaussian form. The maximum current magnitude, current width, and across-channel location of the current maxima were varied. Despite differences in the details of the response, e.g., the extent of the reversal in flow observed during peak winds, general features discussed above hold for any reasonable representation of the current. Although we allow for realistic across-shelf topography and stratification, we acknowledge that the physical geometry of the region is extremely complex and three-dimensional (i.e., canyon and corner in the coastline). Fortunately, the AUV transect location is upstream (in a coastally trapped wave sense) of a large portion of this variability, so that the channel construct may be applicable. A more realistic modeling effort that closely examines the across-shelf circulation should be the focus of future work.

[50] The use of a restoration region is intended to force flow in the same way the large-scale pressure gradient drives flow through the Bering Strait. For a steady system, bottom stress must be balanced in the alongshelf momentum equation, and the alongshelf pressure gradient has been attributed with this role in a variety of regions [e.g., *Huyer*, 1983; *Lentz*, 2008; *Pringle and Dever*, 2009]. It is interesting to note that in each of these cases the alongshelf pressure gradient is in the direction of coastal wave propagation as is true with our model, although in each case the source of the alongshelf pressure gradient is a result of different phenomena. An alternative set up for our model could be developed by imposing an alongshelf pressure gradient acting in the positive x direction (similar to that found downstream of the restoration region) as opposed to forcing the alongshelf current.

[51] The model supports our interpretation that the across-shelf structure is driven by the winds. However, a noticeable deficiency is that the model is not configured to reproduce the meltwater intrusion or the well-defined current core observed in the Peak Wind state, because we have neglected the across-shelf variability in the hydrographic structure necessary to reproduce these features. That being said, the across-shelf velocity response to wind forcing combined with an across-shelf gradient in ice cover suggests a mechanism by which the meltwater intrusion could have formed.

[52] Sea ice data from 23 August 2005 (not shown) reveal the presence of ice less than 10 km from the offshore end of the AUV transect line (despite the fact that ice was not present directly over the transect line during AUV operations), providing an offshore source of relatively cold, fresh water necessary to produce the observed intrusion. Across-shelf and alongshelf winds are directed so that both components yielded a near-surface offshore flow, which would tend to drive floating sea ice further offshore. At the same time, the return flow at the base of the mixed layer (Figure 12b) would support the onshore movement of MW. Lateral gradients in temperature and salinity induced by ice cover offshore and warm ACC water onshore create the possibility that across-shelf winds (as opposed to only alongshelf winds) may be playing a role in redistribution of TS properties, even in regions where the surface Ekman layer is well separated from the bottom Ekman layer.

[53] The observed shift in coastal current structure not only influences the TS properties of the transport (section 5.1), thus potentially influencing downstream hydrographic conditions, but also the structure and stability of the along-shelf current. Figure 13 shows the relative vorticity for the current measured during the three wind states. Differences in the across-shelf structure are easily observed in comparison of the relative vorticity fields. In particular, the anticyclonic vorticity found on the shoreward side of the current core was much stronger during the Peak Wind state as compared to either Post Wind state, an attribute that has potential relevance to the stability of the current.

[54] Anticyclonic eddies are found throughout the Canada Basin [e.g., *Manley and Hunkins*, 1985]. In the southern Beaufort Sea, these eddies typically are found around 100 m depth with widths of O(10 km); detailed observations have shown that the relative vorticity in eddy cores is roughly $-f$ [*D'Asaro*, 1988b]. Previous studies have suggested that Barrow Canyon may be a region of eddy formation [*D'Asaro*, 1988a; *Watanabe and Hasumi*, 2009], and *D'Asaro* [1988a] proposed that the frictional boundary layer along the shoreward side of the canyon could reduce the potential vorticity to a value consistent with that observed within the eddies. Observational studies [*Pickart et al.*, 2005; *Münchow and Carmack*, 1997], however, have found anticyclonic shear is too small to account for the necessary reduction in total vorticity. As an alternate mechanism, *Spall et al.* [2008] show that eddies may be formed via baroclinic instability further downstream along the Beaufort Slope.

[55] In contrast to previous data sets, these data show that in the Peak Wind and Post Wind II states the relative vorticity ($-\partial u/\partial y$) on the shoreward edge of the domain was less than $-f$ (Figures 13a and 3c). For both of these transects the measured relative vorticity reached a minimum value of $\sim -2 \times f$; however, the anticyclonic region was deeper and extended over a greater area in the Peak Wind state. These data do not allow for evaluation of a formation process, and the observed temperatures are warmer than those typically observed in the Beaufort Gyre eddies [*Manley*

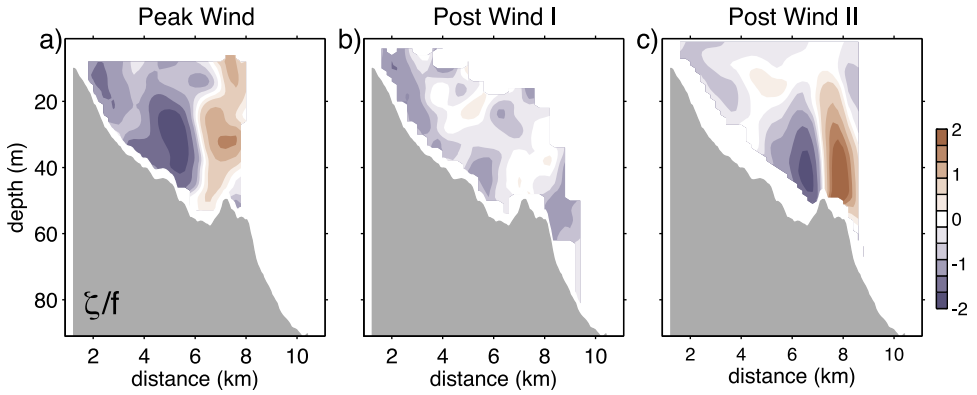

Figure 13. Relative vorticity for (a) Peak Wind, (b) Post Wind I, and (c) Post Wind II states.

and Hunkins, 1985]. However, these observations suggest that sufficiently low potential vorticity may be found very close to shore (at least during some forcing scenarios) to support the formation mechanism suggested by *D'Asaro* [1988a].

7. Summary

[56] Four across-shelf transects obtained with a REMUS-100 AUV were used in conjunction with a process-oriented numerical model to diagnose wind-driven circulation in the Alaskan coastal current along the eastern flank of Barrow Canyon. These high-resolution data are particularly useful in this region, as it is (1) difficult to sample due to environmental factors and (2) characterized by high variability and small internal deformation radius. The transects were identified according to their timing relative to two isolated wind events. Both wind events were upwelling favorable, but also included a substantial offshore component. One transect was obtained near the peak of the first event, two back-to-back transects were obtained just as the second wind event ended, and one transect was obtained several days after the peak of the first event. The transects were designated Peak Wind, Post Wind I, and Post Wind II, respectively.

[57] This data set demonstrates that even over the course of a week the hydrographic and current structure can vary markedly. Of interest in the Peak Wind transect was the appearance of middepth mixed meltwater intrusion approximately 7 km offshore, which was not observed in other transects. The Peak Wind state was also distinguished by the presence of a subsurface poleward jet with core speed of 0.75 m s^{-1}. The alongshelf flow in both Post Wind states was also poleward with typical speeds of 0.4–0.5 m s^{-1}; however, a jet-like structure was not evident in these cases. Alongshelf transports integrated to 8 km offshore, were consistent among the three states, with transports of ~0.12 Sv of which 40–50% was Alaskan Coastal Current water. In the Peak Wind state, the transport-weighted average temperature was about 1°C cooler than the two postwind states.

[58] To test the hypothesis that differences in hydrographic structure, and in particular the presence of the MW intrusion, could be accounted for by wind forcing, an idealized model was used to study the influence of a moderate upwelling wind event on a "background" coastal current that flows counter to the alongshelf winds. For the given stratification, wind forcing, and topography, the model predicts that return flow occurs both at the base of the surface Ekman layer and diffusely in the interior of the water column. Over the region in which the coastal current does not reverse, flow in the bottom boundary layer is offshore, in the same direction as that of the surface Ekman layer, since it is set by the frictional response to the interior current. In addition, upwelling of isopycnals is more pronounced in the nearshore, and in deeper water isopycnals turn down into the bottom boundary layer consistent with the thermal wind shear of the mean flow. The model appears to reasonably capture the general character of the AUV observations. Furthermore, the location of the maximum return flow is consistent with the location of the meltwater intrusion, suggesting that the wind-driven, across-shelf circulation may indeed play a role in driving MW shoreward.

[59] For the Peak Wind and Post Wind II states, the relative vorticity was less than $-f$ on the shoreward side of the current. This result is of interest in that it shows the plausibility of an eddy generation mechanism proposed by *D'Asaro* [1988a], which has not been supported by prior observations. The existence of a strong, anticyclonic vorticity in these data may be attributed to the resolution and range provided by the AUV, the wind state, or some combination of the two. Future work should include a study aimed at understanding how the wind state influences the across-shelf vorticity structure, and what implications this effect may have to stability of the current.

[60] **Acknowledgments.** The AUV observations were made possible by the efforts of G. Packard, J. Lord, and A. Shcherbina. Field operations were coordinated through the Barrow Arctic Science Consortium. The AUV support boat was operated by the Native Village of Barrow. Field work and analysis (A.J.P.) was supported by the Comer Science Education Foundation and the WHOI Ocean and Climate Change Institute. E.L.S. was supported as a WHOI Postdoctoral Scholar. G. Gawarkiewicz helped develop the observational approach. R. Pickart provided valuable feedback that improved the analysis.

References

Aagaard, K., and A. T. Roach (1990), Arctic ocean-shelf exchange: Measurements in Barrow Canyon, *J. Geophys. Res.*, *95*(C10), 18,163–18,175, doi:10.1029/JC095iC10p18163.

Allen, J. S. (1973), Upwelling and coastal jets in a continuously stratified ocean, *J. Phys. Oceanogr.*, *3*, 245–257, doi:10.1175/1520-0485(1973)003<0245:UACJIA>2.0.CO;2.

Austin, J. A., and S. J. Lentz (2002), The inner shelf response to wind-driven upwelling and downwelling, *J. Phys. Oceanogr.*, *32*(7), 2171–2193, doi:10.1175/1520-0485(2002)032<2171:TISRTW>2.0.CO;2.

Barth, J. A., S. D. Pierce, and R. M. Castelao (2005), Time-dependent, wind-driven flow over a shallow midshelf submarine bank, *J. Geophys. Res.*, *110*, C10S05, doi:10.1029/2004JC002761.

Chapman, D. C., and S. J. Lentz (1997), Adjustment of stratified flow over a sloping bottom, *J. Phys. Oceanogr.*, *27*, 340–356, doi:10.1175/1520-0485(1997)027<0340:AOSFOA>2.0.CO;2.

Chapman, D. C., and S. J. Lentz (2005), Acceleration of a stratified current over a sloping bottom, driven by an alongshelf pressure gradient, *J. Phys. Oceanogr.*, *35*, 1305–1317, doi:10.1175/JPO2744.1.

Coachman, L. K., K. Aagaard, and R. B. Tripp (1975), *Bering Strait: The Regional Physical Oceanography*, Univ. of Wash. Press, Seattle.

D'Asaro, E. A. (1988a), Generation of submesoscale vortices: A new mechanism, *J. Geophys. Res.*, *93*(C6), 6685–6693, doi:10.1029/JC093iC06p06685.

D'Asaro, E. A. (1988b), Observations of small eddies in the Beaufort Sea, *J. Geophys. Res.*, *93*(C6), 6669–6684, doi:10.1029/JC093iC06p06669.

Davis, R. E., and P. S. Bogden (1989), Variability on the California Shelf forced by local and remote winds during the Coastal Ocean Dynamics Experiment, *J. Geophys. Res.*, *94*(C4), 4763–4783, doi:10.1029/JC094iC04p04763.

Dever, E. P. (1997), Wind-forced cross-shelf circulation on the northern California shelf, *J. Phys. Oceanogr.*, *27*, 1566–1580, doi:10.1175/1520-0485(1997)027<1566:WFCSCO>2.0.CO;2.

Fewings, M., S. J. Lentz, and J. Fredericks (2008), Observations of cross-shelf flow driven by cross-shelf winds on the inner continental shelf, *J. Phys. Oceanogr.*, *38*, 2358–2378, doi:10.1175/2008JPO3990.1.

Fong, D. A., and W. R. Geyer (2001), Response of a river plume during an upwelling favorable wind event, *J. Geophys. Res.*, *106*(C1) 1067–1084, doi:10.1029/2000JC900134.

Fong, D. A., W. R. Geyer, and R. P. Signell (1997), The wind-forced response on a buoyant coastal current: Observations of the western Gulf of Maine plume, *J. Mar. Syst.*, *12*, 69–81, doi:10.1016/S0924-7963(96)00089-9.

Gan, J., and J. S. Allen (2002), A modeling study of shelf circulation off northern California in the region of the Coastal Ocean Dynamics Experiment: Response to relaxation of upwelling winds, *J. Geophys. Res.*, *107*(C9), 3123, doi:10.1029/2000JC000768.

García-Reyes, M., and J. Largier (2010), Observations of increased wind-driven coastal upwelling off central California, *J. Geophys. Res.*, *115*, C04011, doi:10.1029/2009JC005576.

Garrett, C. J., P. B. Rhines, and P. Maccready (1993), Boundary mixing and arrested Ekman layers: Rotating stratified flow near a sloping boundary, *Annu. Rev. Fluid Mech.*, *25*, 291–321, doi:10.1146/annurev.fl.25.010193.001451.

Garrison, G. R., and R. G. Paquette (1982), Warm water interactions in the Barrow Canyon in winter, *J. Geophys. Res.*, *87*(C8), 5853–5859, doi:10.1029/JC087iC08p05853.

Hickey, B., S. Geier, N. Kachel, and A. MacFadyen (2005), A bi-directional river plume: The Columbia in summer, *Cont. Shelf Res.*, *25*, 1631–1656, doi:10.1016/j.csr.2005.04.010.

Huyer, A. (1983), Coastal upwelling in the California current system, *Progr. Oceanogr.*, *12*, 259–284, doi:10.1016/0079-6611(83)90010-1.

Large, W. G., J. C. McWilliams, and S. C. Doney (1994), Oceanic vertical mixing: A review and a model with a nonlocal boundary layer parameterization, *Rev. Geophys.*, *32*, 363–404, doi:10.1029/94RG01872.

Lentz, S. J. (2001), The influence of stratification on the wind-driven cross-shelf circulation over the North Carolina shelf, *J. Phys. Oceanogr.*, *31*, 2749–2760, doi:10.1175/1520-0485(2001)031<2749:TIOSOT>2.0.CO;2.

Lentz, S. (2004), The response of buoyant coastal plumes to upwelling-favorable winds, *J. Phys. Oceanogr.*, *34*, 2458–2469, doi:10.1175/JPO2647.1.

Lentz, S. J. (2008), Observations and a model of the mean circulation over the Middle Atlantic Bight continental shelf, *J. Phys. Oceanogr.*, *38*, 1203–1221, doi:10.1175/2007JPO3768.1.

Lentz, S. J., and D. C. Chapman (2004), The importance of nonlinear cross-shelf momentum flux during wind-driven coastal upwelling, *J. Phys. Oceanogr.*, *34*, 2444–2457, doi:10.1175/JPO2644.1.

Lentz, S. J., and C. D. Winant (1986), Subinertial currents on the southern Califoinia shelf, *J. Phys. Oceanogr.*, *16*, 1737–1750, doi:10.1175/1520-0485(1986)016<1737:SCOTSC>2.0.CO;2.

Manley, T. O., and K. Hunkins (1985), Mesoscale eddies of the Arctic Ocean, *J. Geophys. Res.*, *90*(C3), 4911–4930, doi:10.1029/JC090iC03p04911.

Marshall, J., A. Adcroft, C. Hill, L. Perelman, and C. Heisey (1997), A finite-volume, incompressible Navier Stokes model for studies of the ocean on parallel computers, *J. Geophys. Res.*, *102*(C3), 5753–5766, doi:10.1029/96JC02775.

Mountain, D. G., L. K. Coachman, and K. Aagaard (1976), On the flow through Barrow Canyon, *J. Phys. Oceanogr.*, *6*, 461–470, doi:10.1175/1520-0485(1976)006<0461:OTFTBC>2.0.CO;2.

Münchow, A., and E. C. Carmack (1997), Synoptic flow and density observations near an Arctic Shelf Break, *J. Phys. Ocean.*, *27*, 1402–1419, doi:10.1175/1520-0485(1997)027<1402:SFADON>2.0.CO;2.

Münchow, A., and R. W. Garvine (1993), Buoyancy and wind forcing of a coastal current, *J. Mar. Res.*, *51*(2), 293–322.

Okkonen, S. R., C. J. Ashjian, R. G. Campbell, W. Maslowski, J. L. Clement-Kinney, and R. Potter (2009), Intrusion of warm Bering/Chukchi waters onto the shelf in the western Beaufort Sea, *J. Geophys. Res.*, *114*, C00A11, doi:10.1029/2008JC004870. [Printed *115*(C1), 2010.]

Paquette, R. G., and R. H. Bourke (1974), Observations on the coastal current of Arctic Alaska, *J. Mar. Res.*, *32*(2), 195–207.

Pickart, R. S., T. J. Weingartner, L. J. Pratt, S. Zimmermann, and D. J. Torres (2005), Flow of winter-transformed Pacific water into the western Arctic, *Deep Sea Res., Part II*, *52*, 3175–3198, doi:10.1016/j.dsr2.2005.10.009.

Pringle, J. M. (2002), Enhancement of wind-driven upwelling and downwelling by alongshore bathymetric variability, *J. Phys. Oceanogr.*, *32*, 3101–3112, doi:10.1175/1520-0485(2002)032<3101:EOWDUA>2.0.CO;2.

Pringle, J. M., and E. P. Dever (2009), Dynamics of wind-driven upwelling and relaxation between Monterey Bay and Point Arena: Local-, regional-, and gyre-scale controls, *J. Geophys. Res.*, *114*, C07003, doi:10.1029/2008JC005016.

Roach, A. T., K. Aagaard, C. H. Pease, S. A. Salo, T. Weingartner, V. Pavlov, and M. Kulakov (1995), Direct measurements of transport and water properties through the Bering Strait, *J. Geophys. Res.*, *100*(C9), 18,443–18,457, doi:10.1029/95JC01673.

Spall, M. A. (2007), Circulation and water mass transformation in a model of the Chukchi Sea, *J. Geophys. Res.*, *112*, C05025, doi:10.1029/2005JC003364.

Spall, M. A., R. S. Pickart, P. S. Fratantoni, and A. J. Plueddemann (2008), Western Arctic shelfbreak eddies: Formation and transport, *J. Phys. Oceanogr.*, *38*, 1644–1668, doi:10.1175/2007JPO3829.1.

Tilburg, C. E. (2003), Across-shelf transport on a continental shelf: Do across-shelf winds matter?, *J. Phys. Oceanogr.*, *33*, 2675–2688, doi:10.1175/1520-0485(2003)033<2675:ATOACS>2.0.CO;2.

Walsh, J., et al. (1989), Carbon and nitrogen cycling within the Bering/Chukchi seas: Source regions for organic matter effecting AOU demands of the Arctic Ocean, *Prog. Oceanogr.*, *22*(4), 277–359, doi:10.1016/0079-6611(89)90006-2.

Watanabe, E., and H. Hasumi (2009), Pacific water transport in the western Arctic Ocean simulated by an eddy-resolving coupled sea ice-ocean model, *J. Phys. Oceanogr.*, *39*, 2194–2211, doi:10.1175/2009JPO4010.1.

Weingartner, T. J., D. J. Cavalieri, K. Aagaard, and Y. Sasaki (1998), Circulation, dense water formation, and outflow on the northeast Chukchi shelf, *J. Geophys. Res.*, *103*(C4), 7647–7662, doi:10.1029/98JC00374.

Weingartner, T., K. Aagaard, R. Woodgate, S. Danielson, Y. Sasakic, and D. Cavalieri (2005), Circulation on the north central Chukchi Sea shelf, *Deep Sea Res., Part II*, *52*, 3150–3174, doi:10.1016/j.dsr2.2005.10.015.

Whitney, M. M., and J. S. Allen (2009), Coastal wind-driven circulation in the vicinity of a bank. Part II: Modeling flow over the Heceta Bank complex on the Oregon coast, *J. Phys. Oceanogr.*, *39*, 1298–1316, doi:10.1175/2008JPO3967.1.

Whitney, M. M., and R. W. Garvine (2005), Wind influence on a coastal buoyant outflow, *J. Geophys. Res.*, *110*, C03014, doi:10.1029/2003JC002261.

Winant, C. D. (1980), Coastal circulation and wind-induced currents, *Annu. Rev. Fluid Mech.*, *12*, 271–301, doi:10.1146/annurev.fl.12.010180.001415.

Winsor, P., and D. C. Chapman (2004), Pathways of Pacific water across the Chukchi Sea: A numerical model study, *J. Geophys. Res.*, *109*, C03002, doi:10.1029/2003JC001962.

Woodgate, R. A., and K. Aagaard (2005), Revising the Bering Strait freshwater flux into the Arctic Ocean, *Geophys. Res. Lett.*, *32*, L02602, doi:10.1029/2004GL021747.

Woodgate, R. A., K. Aagaard, and T. J. Weingartner (2005), A year in the physical oceanography of the Chukchi Sea: Moored measurements from autumn 1990–1991, *Deep Sea Res., Part II*, *52*, 3116–3149, doi:10.1016/j.dsr2.2005.10.016.

A. J. Plueddemann, Woods Hole Oceanographic Institution, 266 Woods Hole Rd., MS 29, Woods Hole, MA 02543, USA. (aplueddemann@whoi.edu)

E. L. Shroyer, College of Earth, Ocean, and Atmospheric Sciences, Oregon State University, 104 COAS Administration Bldg., Corvallis, OR 97331, USA. (eshroyer@coas.oregonstate.edu)